Self-Interference Cancellation Enabling High-Throughput Short-Reach Wireless Full-Duplex Communication

Haolin Li, *Student Member, IEEE*, Joris Van Kerrebrouck, *Student Member, IEEE*, Olivier Caytan, *Student Member, IEEE*, Hendrik Rogier, *Senior Member, IEEE*, Johan Bauwelinck, *Senior Member, IEEE*, Piet Demeester, *Fellow, IEEE*, and Guy Torfs, *Member, IEEE*

***Abstract*— In-band full-duplex (FD) wireless communication allows the simultaneous transmission and reception of data at the same frequency band, effectively doubling the spectral efficiency and data rate while reducing the latency. Previously published designs mostly target the self-interference (SI) cancellation in conventional wireless systems. In this paper, we focus on real-time SI cancellation for short-reach wireless FD systems. The superior signal quality of a point-to-point short-reach wireless system, allows the utilization of wideband communications to achieve a high throughput. Besides, in such wireless systems, the impacts of phase noise and nonlinear distortions are largely reduced, easing the SI cancellation. Moreover, the degradation of signal reception quality due to FD operation is experimentally evaluated in different environments. Experimental results of a prototype implementation show that a combination of antenna isolation and digital cancellation can already achieve an overall SI cancellation performance of 72.5 dB over a bandwidth of 123 MHz. This prototype can support a high-data-rate FD communication link of close to 1 Gbps up to 300 cm with an error vector magnitude lower than −26 dB in a typical indoor environment.**

***Index Terms*— Digital cancellation, in-band full-duplex, self-interference, short-reach wireless, wideband, indoor.**

I. Introduction

FULL-DUPLEX (FD) wireless communication offers the potential of increasing spectral efficiency, doubling the physical layer capacity and reducing the air interface delay and latency [1], [2]. Moreover, full-duplex communication enables the channel reciprocity, being transmission and reception at the same frequency band at the same time. These features make it an appealing concept to increase the data rates of the individual users envisioned in 5G communication systems [3]. Specifically, these FD benefits can be exploited in short-reach wireless communication systems. Compared to conventional wireless systems, the requirements for high throughput and low latency are usually more stringent in short-reach wireless systems. For instance, the reduced latency owing to full-duplex operation, can take the virtual-reality (VR) experience to the next level. In addition, high-throughput short-reach wireless FD connections are also very attractive for applications such as wireless peer-to-peer communication [4], [5], close wireless proximity [6] and wireless USB [7].

The key challenge of such in-band FD systems lies in canceling the strong self-interference (SI). The self-interference signal is inflicted by the local transmitter upon its own local receiver through the SI coupling channel. This SI signal overlaps with the received signal of interest in the same frequency band and time slot, thereby interfering with the reception of the signal of interest. In conventional wireless systems, more than 100 dB of self-interference cancellation is required to achieve the same signal-to-noise-plus-interference ratio (SNIR) of its half-duplex (HD) counterpart [2], [8], [9]. A combination of different cancellation techniques is usually needed to achieve this amount of cancellation. As such, SI cancellation techniques can be classified into three categories: antenna isolation [8], [10]–[17], analog RF (or baseband) cancellation [8], [18], [19] and digital cancellation [10], [12], [20]–[22].

Recently, some full-duplex radio demonstrations have been reported in literature [10], [12], [20], [23]. In these papers, both analog RF (or baseband) cancellation and digital baseband cancellation were proposed for SI suppression. However, these papers target conventional wireless systems in which the system bottlenecks and challenges are quite different from those in short-reach wireless systems. The analytical and experimental results in [24]–[30] and comprehensive surveys in [2] and [9] reveal that transceiver RF impairments such as phase noise and power amplifier (PA) nonlinearities, SI channel estimation error and the limited resolution of analog-to-digital converters (ADCs) are the main performance limiting factors in conventional FD systems. In contrast, in short-reach wireless systems, the signal of interest experiences less path loss and the transmit power is usually lower. Therefore, the signal of interest is not masked by transceiver nonlinear distortions. Simulation results in [26] show that in the common oscillator scenario, even though most of the phase noise is canceled by the downconverting oscillator,

Manuscript received November 30, 2017; revised April 26, 2018; accepted July 9, 2018. Date of publication August 2, 2018; date of current version October 9, 2018. This work was supported by the ERC Advanced Grant ATTO Project under Grant 695495. The associate editor coordinating the review of this paper and approving it for publication was S. Kompella. *(Corresponding author: Haolin Li.)*

The authors are with the IDLab, Department of Information Technology (INTEC), Ghent University–imec, 9052 Ghent, Belgium (e-mail: haolin.li@ugent.be; guy.torfs@ugent.be; johan.bauwelinck@ugent.be).

Color versions of one or more of the figures in this paper are available online at http://ieeexplore.ieee.org.

Digital Object Identifier 10.1109/TWC.2018.2859985

the phase noise increases the noise floor by 4 to 5 dB. However, the higher signal quality in short-reach wireless systems, can tolerate this increased noise floor. Besides, the superior signal quality enables the utilization of wideband communications to boost the throughput. Moreover, previous works have mostly focused on SI cancellation techniques in the absence of the desired signal or have commonly assumed that the SI channel estimation is done prior to the real communication of two FD radio nodes. This obviously lowers the total achievable data rate, as periodical estimation is mandatory because in most cases the SI channels are time-varying. The channel variation over time will erode the accuracy of SI channel estimation or even make pre-estimation of the SI channel impractical. The main contributions of this paper are the following:

- Real-time self-interference cancellation is demonstrated. The feasibility of such wireless FD systems using only a combination of antenna isolation and digital cancellation is experimentally validated in different environments.
- The impact of the signal of interest on SI cancellation is analyzed. When the SI digital cancellation and the reception of the signal of interest are performed simultaneously, the self-interference cannot be totally canceled. The degradation of signal reception quality owing to the FD operation is experimentally evaluated.
- The experimentally achieved throughput in a typical indoor environment exceeds that of previous publications: close to 1.5 Gbps up to 200 cm distance with an error vector magnitude (EVM) lower than -25 dB or close to 1 Gbps up to 300 cm with an EVM lower than -26 dB for single-carrier (SC) signals. As for orthogonal frequency-division multiplexing (OFDM) signals, the achieved throughput is 884.74 Mbps at 300 cm distance with -23.2 dB EVM.

The remainder of this paper is organized as follows: Section II discusses short-reach wireless full-duplex systems and the impact of various impairments to analyze the feasibility of such systems. In Section III, the basic model and cancellation principle of self-interference are described. Details are given about channel estimation algorithms and the synchronization for the implementation of FD transceivers. Section IV describes the hardware implementation of the major building blocks for SI cancellation. Section V discusses the experimental verification of the real-time system in different environments and test conditions. Finally, conclusions are drawn in Section VI.

II. Short-Reach Wireless Full-Duplex Communication Systems

Short-reach wireless communication systems are typically limited to a range of several meters and aim to set up a point-to-point direct communication link. In contrast to conventional wireless communications, such systems usually have a high signal quality owing to the directional communication and low path loss, reducing the required transmit power. Machine-to-machine (M2M), Internet of Things (IoT) [31] and entertainment, are envisioned application areas of such wireless systems. VR and laptop wireless docking stations are typical application scenarios in daily life.

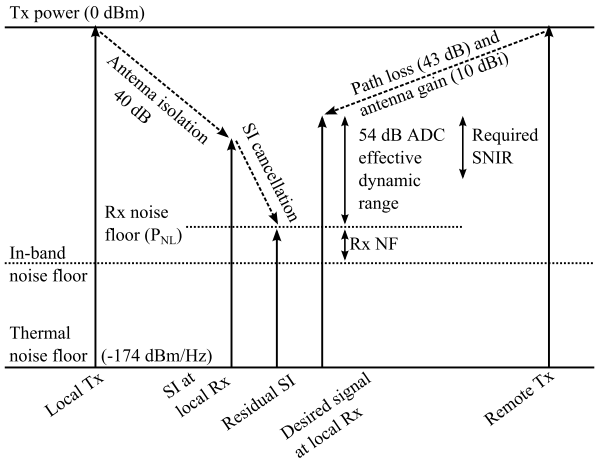

Fig. 1. Illustration of various in-band power levels in a full-duplex link budget for a point-to-point communication link at 100 cm distance.

In this paper, we consider an application scenario of two devices in a point-to-point full-duplex system operating over a short distance (denoted as local node and remote node). The feasibility analysis of such systems is firstly focused on SC modulations, then the system performance evaluation is also extended for multi-carrier modulations. Fig. 1 illustrates the power levels of different signals in such a system at a distance of 100 cm. The transmit power is limited to 0 dBm. Therefore, the PA nonlinear distortion is not a concern even for high-order QAM modulation schemes, where high linearity is required for large peak-to-average power ratio (PAPR). The signal strength of the desired signal P_{r} impinging on the local receiver is -33.32 dBm for a frequency of 3.5 GHz and an antenna gain of 5 dBi for both transmit and receive antennas. For a targeted bit error rate (BER) of 10^{-5}, at least 25.5 dB SNIR is required for 64-QAM modulated signals [32]. An increase in signal bandwidth directly leads to an increased in-band receiver noise floor P_{NL} or a reduction in SNIR when the transmit power is fixed. P_{NL} is determined by the in-band thermal noise floor, the receiver noise figure (NF) and the bandwidth B.

$$P_{\mathrm{NL}}\,[\mathrm{dBm}] = -174\left[\frac{\mathrm{dBm}}{\mathrm{Hz}}\right] + 10\log_{10}(B[\mathrm{Hz}]) + NF[\mathrm{dB}], \quad (1)$$

For example, assuming a receiver NF of 5 dB and taking a signal bandwidth B of 200 MHz, yields a receiver noise floor P_{NL} of -85.99 dBm according to (1).

The electrical balance duplexer (EBD) is very attractive for small form factor devices, however, the SI isolation is sensitive to antenna impedance variations in both the frequency domain and time domain, limiting the achievable isolation bandwidth and requiring active tuning of the impedance network. Besides, the use of a hybrid transformer in EBD, causes unavoidable insertion loss [16]. The shared-antenna architecture via a circulator only provides a passive isolation of about 15 dB (antenna reflection dominates) [2], [13]. The separate-antenna architecture achieves a good isolation via propagation loss only

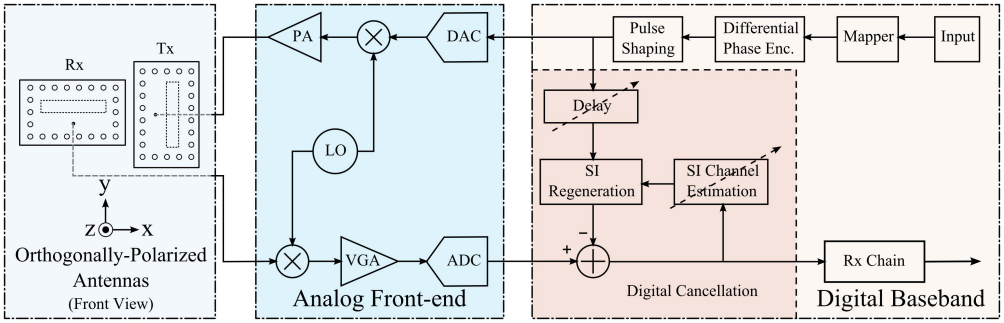

Fig. 2. The full-duplex transceiver architecture including orthogonally-polarized antennas and blind adaptive linear digital self-interference cancellation. The digital baseband of single-carrier modulation is illustrated, however, the digital cancellation algorithm is also applicable for multi-carrier modulations.

when the antennas are separated by a large distance. Therefore, the transceiver architecture of the radio node exploits the antenna polarization as illustrated in Fig. 2, aiming to increase antenna isolation and isolation bandwidth while keeping a relative compact architecture. This orthogonally-polarized-antenna architecture employs a passive isolation scheme to reduce SI leakage into the receiver signal path. The transmit and receive antennas are two identical linearly-polarized slot antennas that are rotated by 90° with respect to each other, being vertically polarized and horizontally polarized, respectively. Owing to this polarization mismatch, the SI can be suppressed by more than 40 dB.

When calculating the ADC's dynamic range, some margin for gain control, quantization noise, PAPR and constructive multipath effects should be taken into account. A 14-bit ADC with eleven effective number of bits (ENOB) yields an effective dynamic range of about 6.02(ENOB-2) $\approx$ 54 dB [8]. Here, one bit (approximately 6 dB) is budgeted to prevent ADC clipping, which depends, among others, on the signal PAPR. Moreover, one additional bit is allocated to prevent the system being limited by quantization noise. An effective dynamic range of 63 dB (PAPR of 4.8 dB is assumed) is found in [28] according to a less conservative approximation.

From the above analysis, it is evident that the remaining self-interference after the antenna isolation stage can already be covered by the ADC's effective dynamic range with respect to the receiver noise floor, as shown in Fig. 1. The nearly equal power level of the SI and the signal of interest at the local receiver input guarantees that the receiver chain is not saturated or desensitized by self-interference and that the signal-of-interest will not be masked by ADC quantization noise.

III. Digital Baseband Self-Interference Cancellation

The goal of digital cancellation is to remove the remaining self-interference after the antenna isolation stage. This section introduces the basic model and cancellation principle of the self-interference. Moreover, the impact of signal of interest on the SI cancellation is described explicitly.

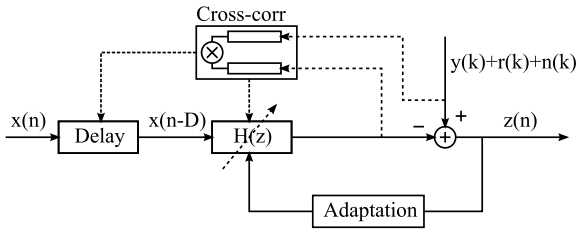

Fig. 3. The general block diagram of blind linear digital cancellation.

A. Basic Modeling and Cancellation Principle

The self-interference signal $y(k)$ can be modeled as a linear function of the baseband transmitted signal, being

$$y(k) = \sum_{i=0}^{N_{\mathrm{SI}}-1} h_{\mathrm{SI},i} x(k-i), \tag{2}$$

where $x(k)$ denotes the complex baseband transmitted signal consisting of in-phase $x_{\mathrm{I}}(k)$ and quadrature $x_{\mathrm{Q}}(k)$ components. $h_{\mathrm{SI},i}$ denotes the complex-valued baseband equivalent of the SI coupling channel impulse response, and k is the sample index. N_{SI} is the length of $h_{\mathrm{SI},i}$. From (2) it is clear that the channel response $h_{\mathrm{SI},i}$ does not take into account potential analog impairments in the signal propagation path from the transmitter baseband to the receiver baseband, such as nonlinear distortion, phase noise and I/Q imbalance [13]. Compared to the signal strength of self-interference and signal of interest, these impairments can be neglected. In this paper, uppercase letters represent frequency-domain signals and lowercase letters represent time-domain signals. Furthermore, the digital baseband signal $r_{\mathrm{Local}}(k)$ at the local Rx can be modeled as

$$r_{\mathrm{Local}}(k) = y(k) + r(k) + n(k), \tag{3}$$

where $r(k)$ is the signal of interest and $n(k)$ represents the additive thermal and quantization noise. As the SI signal $y(k)$ experiences an unknown propagation delay through the SI coupling channel, it should first be synchronized with $x(k)$. Subsequently, the feedforward equalizer (FFE) $H(z)$ (shown in Fig. 3) can be adapted to mimic the SI coupling channel impulse response $h_{\mathrm{SI},i}$. Therefore, the self-interference can be reconstructed in the digital domain by convolving this estimated SI channel impulse response $\hat{h}_i$ with the baseband

signal $x(k)$. The SI generated by the local node can then be subtracted from $r_{\text{Local}}(k)$:

$$z(k) = y(k) + r(k) + n(k) - \sum_{i=0}^{N_{\text{FFE}}-1} \hat{h}_{\text{i}} x(k-i), \tag{4}$$

where $z(k)$ corresponds to the output in Fig. 3. $\hat{h}_i$ and N_{FFE} denote the complex-valued coefficients and the length of FFE $H(z)$, respectively. The canceler output $z(k)$ will be fed to the subsequent baseband receiver chain for further signal processing.

B. Blind Linear Equalizer for Self-Interference Cancellation

Typically, channel estimation may be assisted by training sequences transmitted at the beginning of each data frame. In this paper, the channel estimation employs a fractional-spaced blind equalization technique without any training sequences, where the weights of the equalizer taps are determined in a self-adaptive manner. Therefore, the digital canceler can track the time variations in the SI coupling channel response. To facilitate the real-time processing with low computational complexity, the least-mean-square (LMS) algorithm is adopted for the coefficient adaptation. Since $x(k)$ (or $y(k)$) is uncorrelated with $r(k)$ and $n(k)$, the total power at the local Rx equals the sum of the signal powers of the separate signals. This uncorrelatedness implies also that, in (4), $r(k)$ and $n(k)$ will not be canceled by a linear combination of $x(n)$ [14]. Therefore, minimizing the average power at the output of the digital canceler is equivalent to minimizing the power of self-interference. We define the cost function $J(k)$ of this search algorithm by

$$J(k) = \frac{1}{2} E\{|z(k)^2|\}, \tag{5}$$

where $E\{.\}$ is the expectation. The update of the LMS algorithm is found along the gradient of $J(k)$ with respect to the coefficient $\hat{h}_i$. The LMS algorithm then uses the instantaneous value of $z^2(k)$ at index k as an unbiased estimator of $E\{z^2(k)\}$.

$$\begin{aligned} \frac{\partial J(k)}{\partial \hat{h}_i} &\approx \frac{1}{2} \frac{\partial |z(k)|^2}{\partial \hat{h}_i} \\ &= -z(k) x^*(k-i), \end{aligned} \tag{6}$$

where $z(k)$ is then the instantaneous error and $(.)^*$ denotes the complex conjugate. The update equation is given by

$$\hat{h}_i(k+1) = \hat{h}_i(k) + \mu z(k) x^*(k-i), \tag{7}$$

where μ is the step-size, which controls the tracking rate and the steady-state variance. The convergence properties of the LMS algorithm are governed by μ. $z(k)$ and $x(k)$ will be uncorrelated after convergence.

The complex-valued tap coefficients can resolve the phase error between $x(k)$ and $y(k)$, remove the residual fractional timing error (see Section III-D) and mitigate the signal mismatch due to the multipath effect and the unmatched transmitter pulse shaping. Moreover, by granting the equalizer coefficients sufficient dynamic range, the gain mismatch between $x(k)$ and $y(k)$ can be compensated as well.

In (4), the input of the FFE is the transmitter digital baseband signal $x(k)$, which contains no noise. Therefore, this FFE will not enhance noise.

Compared to the preamble-assisted SI channel estimation, this algorithm requires no orthogonal preambles for different radio nodes. Besides, the cancellation of SI nonlinear components is a significant burden on a real-time system due to the computational complexity when constructing the high-order harmonics of the transmitted baseband signal [22], [33]. By limiting the transmit power in this work, the overhead of either nonlinear digital cancellation or auxiliary Rx chain or pre-calibration proposed in [22] can be avoided. This cancellation algorithm is a linear time-domain approach. As shown in Fig. 2 and the cancellation principle in (4), it only involves the digital baseband signals before the digital-to-analog converter (DAC) and after the ADC, regardless of the used modulation schemes.

C. Impact of Signal of Interest

The uncorrelated received signal of interest $r(k)$ acts as an additional interference source from the perspective of the SI channel estimation, increasing the parameter estimation variance or the number of required iteration steps to achieve a certain level of SI cancellation while maintaining the feedback loop stability. References [21], [34], and [35] have provided an analysis about the impact of the signal of interest on the self-interference cancellation:

$$\text{Var}(\hat{h}_i) \geq \frac{\sigma_{\text{N}}^2 + P_{\text{r}}}{N_{\text{FFE}} P_{\text{SI}}}, \tag{8a}$$

$$0 < \mu < \frac{2}{N_{\text{FFE}}(P_{\text{r}} + P_{\text{SI}} + \sigma_{\text{N}}^2)}, \tag{8b}$$

where $\text{Var}(\hat{h}_i)$ is the estimator variance for each individual tap and σ_{N}^2 is the noise power. $P_{\text{r}} = E[\ |r|^2]$ denotes the average power of the signal of interest and $P_{\text{SI}} = E[\ |y|^2]$ corresponds to the average power of the SI signal before cancellation.

As expressed in (8a), the signal of interest has impact on the estimator variance $\text{Var}(\hat{h}_i)$. Moreover, when the equalizer input power increases due to the presence of the signal of interest, according to (8b), a smaller step-size μ should be used to maintain the LMS algorithm's stability [36]. This, in turn, leads to a slower convergence of the canceler equalization. As a consequence, it becomes more difficult to track the time-varying channel, causing SI cancellation degradation. The impact of the signal of interest becomes even more severe when the channel is frequency selective and when higher-order QAM modulation schemes (higher PAPR) are used. Therefore, trade-offs should be made to approach an optimal performance.

D. Synchronization

Synchronization is an essential function in real-time digital self-interference cancellation. Cross-correlation is used to determine the delay between $x(k)$ and $r_{\text{Local}}(k)$. The cross-correlation is given by

$$\gamma_{xy}(m) = \sum_{k=1}^{N} x(k)(y + r + n)^*(m + k), \tag{9}$$

where the N is the sample size over which the cross-correlation is calculated, k is the sample index, and $m \in [-N, N]$ is the lag index. Here, $\gamma_{xy}(m)$ denotes the cross-correlation function for lag index m. We assume that $x(k)$ is uncorrelated with the additive noise sequence $n(k)$, and that $y(k)$ and $r(k)$ are uncorrelated. Due to the unresolved phase error between $x(k)$ and $y(k)$, the imaginary part of cross-correlation is non-zero. Therefore, the power is considered in the delay estimation. The estimated integer time delay D is obtained by

$$D = \underset{m}{\operatorname{argmax}} \, |\gamma_{xy}(m)|^2, \tag{10}$$

It should be noted that, when the self-interference is much lower than the signal of interest (remote node and local node are at a very close distance where the signal strength of the self-interference is, however, not low enough to provide the required SNIR), a very large number of samples should be included to suppress the uncorrelated signals. Care must be taken when implementing the synchronization on FPGA since the algorithm may consume a lot of FPGA resources. However, the time lag can be calibrated when the signal of interest is absent, since the coarse delay only depends on the actual hardware implementation.

Note that, in case of SC modulations, the DAC operates at four times the symbol rate and the ADC operates at twice the symbol rate. As the cross-correlation is performed at the ADC's clock rate, the timing error of the cross-correlation is limited to $(-0.5T_s, +0.5T_s)$, where T_s is the ADC sample period. This allows aligning the two signals by tuning the delay line (implemented as pipelined registers or FIFOs on an FPGA at the ADC clock rate, denoted by "Delay" in Fig. 2 and Fig. 3). Hence, the cross-correlation is calculated to coarsely estimate the propagation delay in ADC sample periods. The signal mismatch caused by this residual fractional timing error can be reduced by the equalizer $H(z)$ in the SI regeneration process.

IV. Hardware Implementation

A. FPGA Implementation of the Digital Canceler

The digital canceler consists of two parts. A cross-correlation-based coarse delay estimator and an FFE. The coarse delay is only related to the actual hardware implementation, as it depends on the ADC / DAC conversion, buffering of the transmitter and receiver in the FPGA and the analog SI propagation path. Hence, it should be estimated only once. Therefore, a sequential implementation is warranted.

As presented in Fig. 4, for each m in (9), the vector V_1 contains N samples of $x(k)$, and V_2 contains N samples of $r_{\text{Local}}(m + k)$. The initial value of V_2 is shifted for increasing m, while the initial value of V_1 remains the same. The products of each sample in V_1 and V_2 are added by an accumulator or integrator, and forwarded to a power calculator when k equals the sample size N. Each power value $|\gamma(m)|^2$ is compared to the previous maximum. Subsequently, the new maximum and its corresponding lag index m are stored to determine the time delay D, as expressed in (10). This process is repeated $2N+1$ times for $m \in [-N, N]$. Only the 16 most

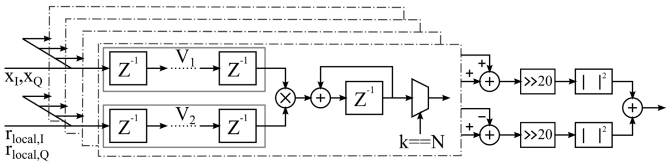

Fig. 4. The block diagram of cross-correlation operation.

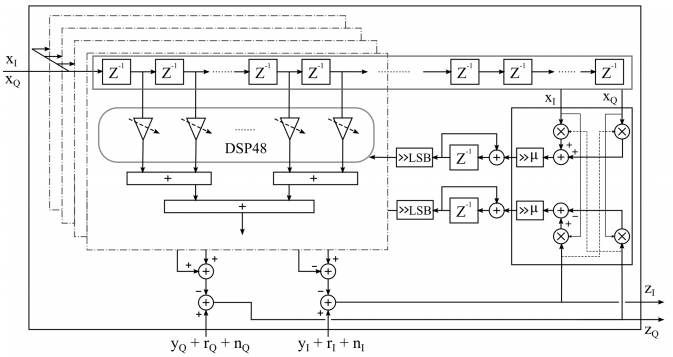

Fig. 5. Block diagram of blind linear equalizer implemented on FPGA. Some extra LSBs are granted for more accurate channel estimation.

significant bits of the accumulator outputs are taken into account to calculate the power. In this way, the number of multipliers is limited to four to evaluate the complex-valued samples and two to compute the power values. The total number of multiplication operations equals $8N^2 + 8N + 2$ (sample products account for $8N^2 + 4N$ operations and the power calculation account for $4N + 2$ operations).

The block diagram of the SI FFE is presented in Fig. 5. The precision of equalizer tap weights has been chosen such that the Xilinx dedicated multiplier IP DSP48 may be exploited while maintaining sufficient accuracy. Each DSP48 can maximally take 25 bits $\times$ 18 bits as inputs. Extra bits (denoted as *LSBs*) may be added to improve the accuracy for the tap adaptation process in (7). These *LSBs* are dropped for the equalization, as expressed in (4). This FFE is essentially a finite-impulse-response (FIR) filter, thus it can be easily pipelined to lower the computation during a single clock cycle. Therefore, the maximal clock frequency of the FPGA implementation is increased to realize a higher throughput.

B. Linearly Polarized Slot Antenna

As mentioned in the previous section, antenna isolation is a key-enabling feature to mitigate self-interference. When employing antennas based on substrate-integrated-waveguide (SIW) technology, their high antenna/platform isolation can be leveraged to achieve a high isolation between transmit and receive antennas.

More specifically, a SIW cavity-backed slot antenna topology [37], [38], depicted schematically in Fig. 6, is adopted. It consists of two conducting layers of copper-plated taffeta electrotextile (sheet resistance 0.2 Ohm/sq), which are attached to a closed-cell expanded-rubber protective-foam layer (dielectric constant $\varepsilon_r = 1.495$, loss tangent $\tan\delta = 0.016$, thickness $= 3.94\,\text{mm}$). An SIW

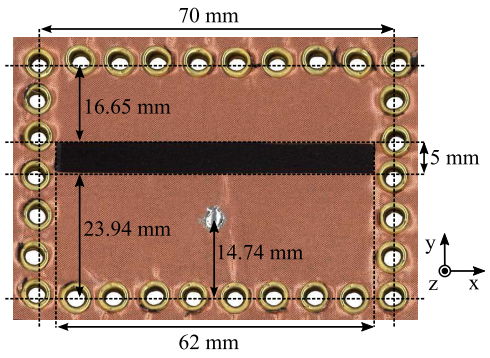

Fig. 6. Substrate-integrated-waveguide cavity-backed slot antenna topology, with dimensions optimized for the 3.5 GHz band.

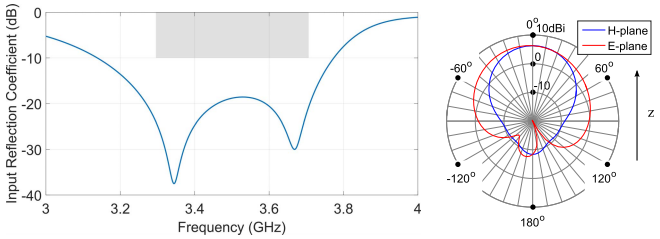

Fig. 7. Simulation results. (a) Input reflection coefficient (dB). (b) Far-field gain pattern in the E-plane and H-plane at 3.5 GHz.

cavity is formed by brass eyelets (outer diameter 4 mm), which interconnect the conducting layers. A slot is cut out of the upper conducting layer, allowing the structure to radiate, and a SubMiniature version A (SMA) connector is used as a coaxial probe to feed the antenna through the bottom conducting ground plane.

Through computer-aided optimization, the antenna is matched to a 50 Ω impedance in the complete 3.3-3.7 GHz band. The optimized dimensions are annotated in Fig. 6. This antenna has been prototyped and characterized. Fig. 7(a) depicts the simulated input reflection coefficients, whereas Fig. 7(b) presents the far-field gain patterns in the E-plane (YZ-plane) and H-plane (XZ-plane). The antenna predominantly radiates in the upper hemisphere ($z > 0$), with a peak gain of 6.47 dBi, linear polarization, and a front-to-back ratio (FTBR) of over 10 dB.

Owing to the high antenna/platform isolation, two antennas of this type can be deployed in the same plane and in close proximity (with a total size smaller than 80 mm × 150 mm), with negligible mutual influence. Their high isolation guarantees almost undisturbed input impedances and radiation patterns in such a setup. Full-wave simulations indicate that, by arranging the transmit and receive antennas as shown in Fig. 8(a), an excellent isolation of over 40 dB is obtained over the entire impedance bandwidth. Fig. 8(b) presents the simulated antenna isolation for this arrangement.

V. Performance Evaluation

In this section, we introduce the experimental setup used to verify the short-reach full-duplex communication system

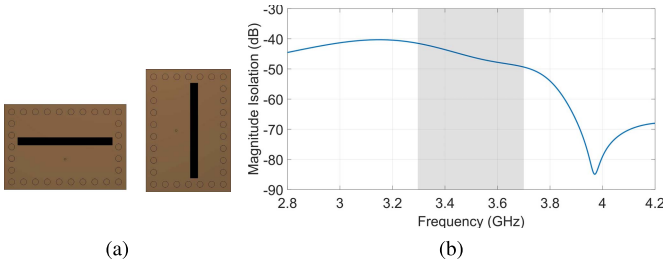

Fig. 8. Transmit and receive antennas. (a) Arrangement for good isolation. (b) Simulated antenna isolation.

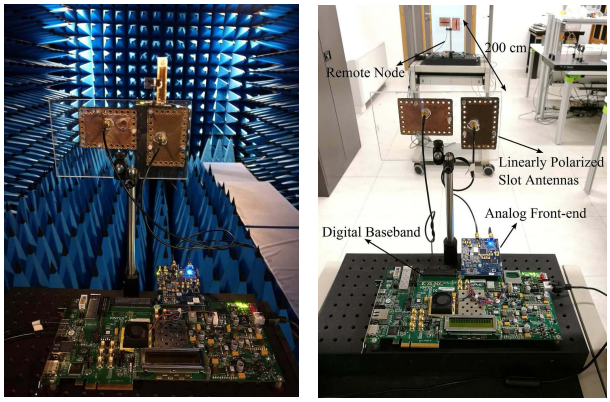

Fig. 9. Experimental setups in the (a) anechoic chamber and (b) indoor environment, composed of Xilinx Kintex 7 FPGAs, analog front-end FMCOMMS1 evaluation kit, and linearly polarized slot antennas.

and the baseband signal processing. The full-duplex system performance is evaluated by comparing the operations in half-duplex and full-duplex modes.

A. Experimental Setup

The measurements are performed in two different environments. The anechoic chamber has (ideally) no reflective objects, while indoor environments are more complicated e.g. including metal closets, radiators and glass doors. The measurement in the anechoic chamber aims to show the optimally achievable performance and to make the measurements repeatable, while the measurement in indoor environments serves to reveal the impact of multipath effects in a FD communication link. As shown in Fig. 9, the measurements involve the analysis of a point-to-point wireless communication link between the local node and the remote node. These radio nodes are located at a height of about 110 cm above the floor with a line-of-sight (LOS) path between antennas. The maximal distances measured are 360 cm and 300 cm in the anechoic chamber and the indoor environment, respectively. Each node can operate either in full-duplex or in half-duplex mode. The remote node transmits the signal of interest. The transmit power of both nodes is 0 dBm and the carrier frequency is centered at 3.5 GHz.

In case of SC modulations, the two nodes do not share the same reference clock, resulting in a small carrier frequency offset. On Fig. 9, one can clearly distinguish the three

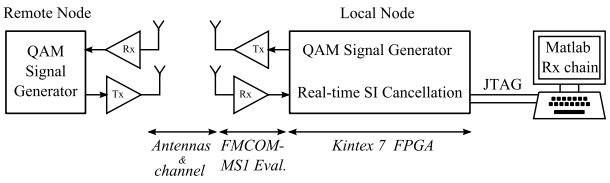

Fig. 10. Block diagram of the experimental setup for SC signals.

main components of the system, being the linearly polarized slot antennas, the analog front-end FMCOMMS1 evaluation kit, and the digital baseband on Xilinx Kintex 7 FPGA. As depicted in the block diagram Fig. 10, the single-carrier signal generation and digital self-interference cancellation are performed in real-time on the Kintex 7 FPGA. The receiver chain is implemented in Matlab, performing, among others, carrier recovery, symbol timing recovery, and equalization. Unless stated otherwise, a baud rate of $R_s = 81.92$ MBaud is transmitted with a square-root-raised-cosine (SRRC) filter with a roll-off factor $\beta = 0.5$, resulting in a bandwidth of $B = R_s(1+\beta) \approx 123$ MHz.

As for the setup of multi-carrier modulations, OFDM signals are generated in Matlab and the digital self-interference cancellation is performed in real-time on FPGA. The OFDM signals are based on the IEEE 802.11g standard: 64-QAM, fast Fourier transform (FFT) size of 64, cyclic prefix size of 16, and 52 sub-carriers (48 data sub-carriers and 4 pilots). Each sub-carrier has 1.536 MHz bandwidth given a sampling rate of 122.88 Msps for both DACs and ADCs. The 52 sub-carriers and one null sub-carrier around DC yield an effective bandwidth of about 81.4 MHz. Note that, unlike the single-carrier's case, two nodes share the same reference clock during this measurement and one preamble per sub-carrier is used for the equalization of the signal of interest.

B. Performance Metrics

We mainly investigate two performance metrics. On the one hand, the SI cancellation capability G measures the maximal SI suppression achieved by the cancellation techniques, when the signal of interest is absent. In practice, the SI digital cancellation and the reception of the signal of interest are performed simultaneously, leading to a potential degradation of signal reception quality. On the other hand, to evaluate the impact of FD operation on signal reception quality, EVM is measured in Matlab to quantify the overall system performance in both HD and FD operation modes. Moreover, to explore the distance and throughput limitation, the EVM measurement is performed at different distances and baud rates, respectively. Unless stated otherwise, the following measurement results are referred to single-carrier signals.

The SI cancellation capability G is defined as the power ratio of the signal power before the SI cancellation to the signal power after the SI cancellation, when the signal of interest is absent [14], [24], [25]:

$$G = \frac{P_{\mathrm{SI}} + \sigma_{\mathrm{N}}^2}{P_{\Delta\mathrm{SI}} + \sigma_{\mathrm{N}}^2}, \tag{11}$$

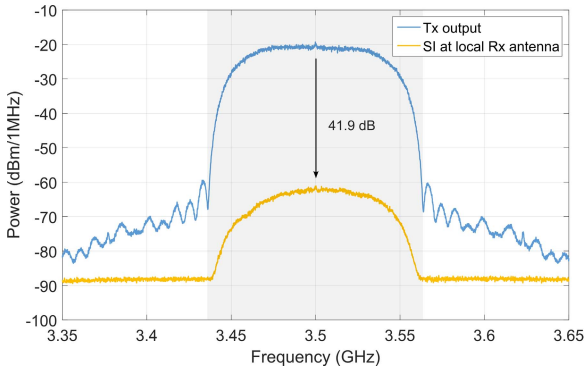

Fig. 11. Different power spectra measured before and after antenna isolation in the indoor environment. The shaded area indicates the integration bandwidth of 123 MHz.

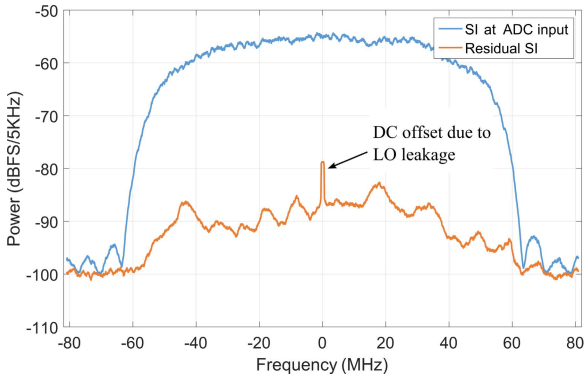

Fig. 12. Power spectra of SI before and after the SI digital cancellation, when the signal of interest is absent. Note that the power is normalized to the ADC dynamic range.

where $P_{\Delta\mathrm{SI}} = E[\,|y_\Delta|^2]$ is the average power of the SI signals after the cancellation.

The root-mean-square (RMS) value of the EVM, EVM_{RMS}, is given by

$$EVM_{\mathrm{RMS}} = \sqrt{\frac{\frac{1}{L}\sum_{k=1}^{L}|\hat{S}_k - S_k|^2}{\frac{1}{L}\sum_{k=1}^{L}|S_k|^2}}, \tag{12}$$

where L is the symbol size taken for averaging, $\hat{S}_k$ and S_k represent the received symbols and the nearest ideal symbols, respectively.

1) SI Cancellation Capability: In indoor environments, the antenna directionality can help to mitigate the multipath effects to some extent. The polarization mismatch provides an antenna isolation of 41.9 dB, as depicted in Fig. 11, which is in good agreement with the simulation shown in Fig. 8. The shaded area indicates the bandwidth of 123 MHz for power integration. The remaining self-interference can be further suppressed by the digital cancellation with a suppression factor of 30.6 dB, as shown in Fig. 12 and Fig. 13. After the digital cancellation, the DC offset due to LO leakage is revealed, as shown in Fig. 12. The DC offset is corrected by the subsequent Rx chain. Note that, in this measurement, variable gain amplification is used to maximize the dynamic range of

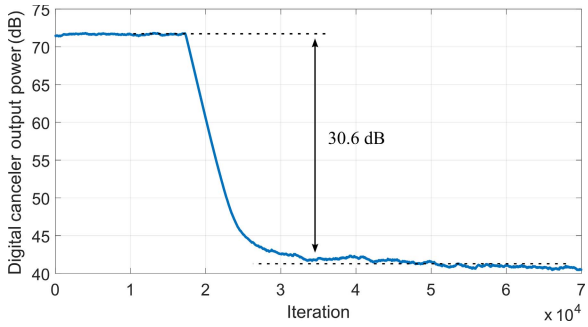

Fig. 13. The averaged power of the digital canceler output signal with respect to the iteration index, when the signal of interest is absent. Each index represents an ADC sample period.

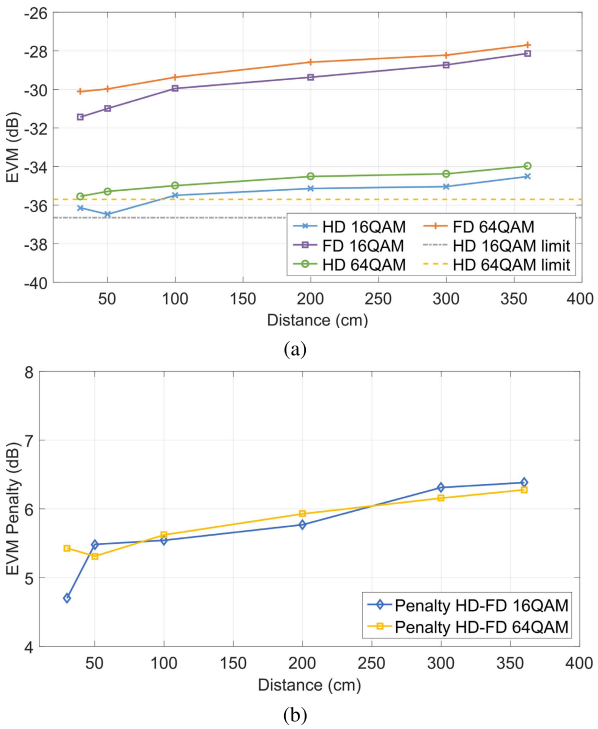

Fig. 14. (a) EVM in half-duplex and full-duplex modes and (b) EVM penalty versus the increased distance in the anechoic chamber.

the ADC. The total self-interference cancellation capability equals approximately 72.5 dB over a 123 MHz bandwidth.

2) Impact of FD Operation on Signal Reception Quality: The EVM is calculated with $L = 50000$ symbols after the equalizer reached a steady-state. The minimum EVM is evaluated in HD mode by connecting two transceivers with an SMA cable. These EVM values are found to be -36.65 dB, for HD 16-QAM, and -35.7 dB, for HD 64-QAM. These values disclose the transceiver performance limitation owing to the analog front-end and the digital baseband implementation.

Fig. 14 shows the EVM variation at different distances in the anechoic chamber. Four measurements are conducted at each distance: HD 16-QAM, FD 16-QAM, HD 64-QAM and FD 64-QAM. In the case of HD 16-QAM and HD 64-QAM, the local node transmitter output is connected to the transmit antenna, however, the output signal is disabled.

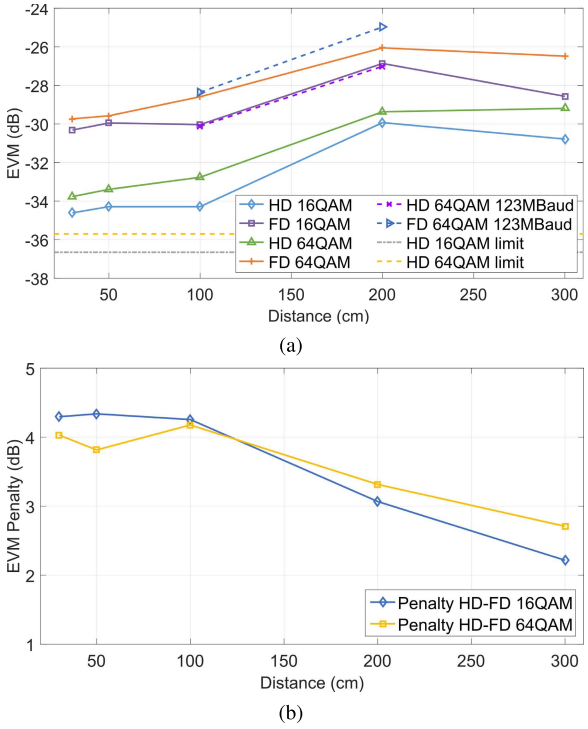

Fig. 15. (a) EVM in half-duplex and full-duplex modes and (b) EVM penalty versus the increased distance in the indoor environment.

Fig. 14(a) reveals that the 16-QAM slightly outperforms 64-QAM in terms of EVM in both modes. As shown in Fig. 14(b), due to self-interference, the EVM penalty between HD 16-QAM and FD 16-QAM is approximately 4.7-6.4 dB. A similar EVM penalty of 5.3-6.3 dB is observed between HD 64-QAM and FD 64-QAM. As the distance increases, the signal of interest becomes weaker, and, hence, the SI is relatively stronger. However, the nearly constant EVM penalty implies that the ADC's effective dynamic range is not degraded by the SI and that the SI suppression increases proportionally with the power of received self-interference, because a higher SI power implies lower channel estimation error and hence better cancellation, as discussed in [14] and [21].

Fig. 15 presents the EVM measurements in the indoor environment. To explore the throughput limitation, different baud rates in the indoor environment are compared. FD 64-QAM 123MBaud represents the full-duplex link of 122.88 MBaud 64-QAM modulated signals (122.88 MBaud corresponds to the maximal ADC rate). A degradation in EVM is observed from 81.92 MBaud to 122.88 MBaud for the 64-QAM modulation in both modes, due to the increase of in-band noise and increased difficulty in digital cancellation and receiver equalization for multipath effects. The effective multipath channel is changing with varying distance between the local and the remote nodes. When the multipath effects cannot be completely eliminated by the equalizers, the measured EVM is dependent upon the location, causing fluctuations in the curves (e.g. EVMs at 200 cm of HD/FD 64-/16-QAM modulations are lower than those at 300 cm). The different results between Fig. 14 and Fig. 15 indicate that the overall system performance in the indoor environment is affected by the type of propagation

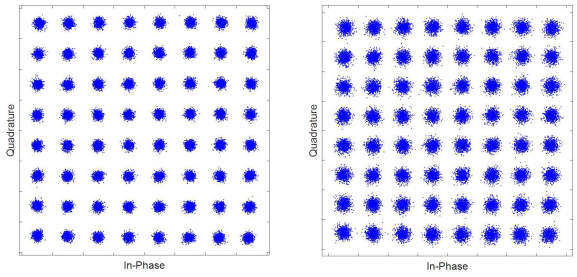

(a) (b)

Fig. 16. The constellation diagrams of 81.92 MBaud 64-QAM signal of interest in the indoor environment at 300 cm distance in (a) half-duplex and (b) full-duplex modes.

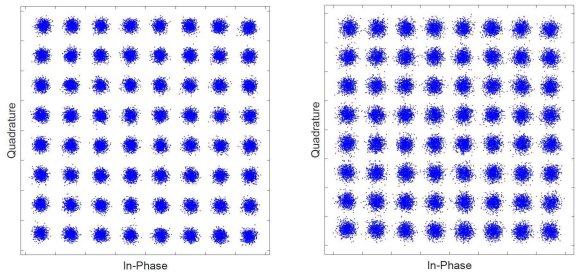

(a) (b)

Fig. 17. The constellation diagrams of 122.88 MBaud 64-QAM signal of interest in the indoor environment at 200 cm distance in (a) half-duplex and (b) full-duplex modes.

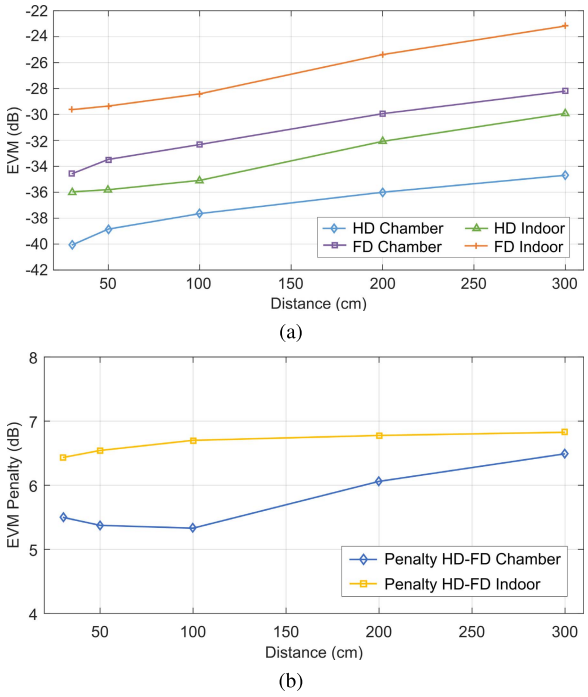

(a)

(b)

Fig. 18. EVM measurements for OFDM signals in the anechoic chamber and indoor environment. (a) EVM in half-duplex and full-duplex modes and (b) EVM penalty versus the increased distance.

environment. It should be pointed out that there is a combined reinforcing effect amongst noise, self-interference and multipath effects in complicated indoor environments. When the distance between two radio nodes increases, the signal of interest's LOS component decreases with respect to the self-interference and the multipath contributions. Fig. 15(b) exhibits a different trend of the EVM penalty, implying that, at larger distances, the multipath effects have a larger impact on the performance than the residual self-interference in case of SC modulations.

For comparison, Fig. 17 shows the measured constellation diagrams of the signal of interest in both half-duplex and full-duplex modes. These measurements are conducted at 300 cm distance and $R_s = 81.92$ MBaud, and at 200 cm distance and $R_s = 122.88$ MBaud, respectively. As shown by the figures, in these cases the constellations are all detectable. Compared to half-duplex modes, the constellation diagrams of full-duplex modes are slightly contaminated due to the reduction in SNIR.

3) Convergence Rate: The convergence of the LMS-based digital canceler, in case of the 64-QAM modulation transmitted over 123 MHz of bandwidth and in the absence of the signal of interest, is illustrated in Fig. 13, which shows its averaged output power for the first 70000 iterations. The canceler equalizer is initialized with a Kronecker delta pulse. It is observed that, to obtain sufficient SI suppression, the LMS algorithm requires approximately 10000 iterations, which roughly corresponds to 61 μs. In this paper, the canceler equalizer has 25 taps. A higher equalizer length N_{FFE} will result in a performance reduction when the canceler adaptation cannot follow the channel variation due to a small step-size μ, as discussed in Section III-C, or when it cannot maintain the LMS algorithm stability.

4) Multi-Carrier Modulation: Fig. 18(a) shows the measured EVM of the OFDM signals averaged over all the measured EVMs per sub-carrier. As shown in Fig. 18(b), OFDM signals have a larger EVM penalty in the anechoic chamber from 5.5 dB to 6.5 dB, even for a smaller bandwidth and shared reference clock. Recall that the penalty for the single-carrier 64-QAM signal is from 5.3 dB to 6.2 dB till 300 cm, as shown in Fig. 14(b). This result follows from the fact that the single-carrier 64-QAM signal has a PAPR of 3.7 dB, while the OFDM signal transmitted has a larger PAPR of 9.3 dB. Therefore, OFDM signals require larger power backoffs for components such as PA, mixers, and ADCs to avoid distortions, this, however, occupies the dynamic ranges of these components. Meanwhile, it is intuitively clear that the digital cancellation converges slower when the signal has a larger PAPR, since the cancellation algorithm minimizes the average output power. The EVM penalty varies from 6.4 dB to 6.8 dB in the indoor environment. Compared to the single-carrier, the measurements of OFDM signals in the anechoic chamber and indoor environment are more consistent as OFDM signals are more efficient against the multipath effects. It should also be mentioned that, for a given (limited) transmit power, the received signal power from the remote node is approaching the receiver noise floor when the distance increases.

5) Overall System Performance: The achieved total throughput of 983.04 Mbps is obtained when a 81.92 MBaud 64-QAM modulated signal is transmitted by both the local

TABLE I
PERFORMANCE COMPARISON AMONG EXISTING SI CANCELLATION TECHNIQUES

Year	Architecture	Platform	Center Frequency	Bandwidth	Cancellation Capability	Throughput	EVM	FD Gain
2012 [39]	Separate antennas	WARP platform	2.4 GHz	40 MHz	74 dB	–	–	–
2013 [13]	Circulator-based single antenna	Rohde and Schwarz (VSG/VSA)/WARP baseband on PC	2.4 GHz	80 MHz	110 dB	–	–	1.87
2015 [10]	Dual-polarization slot antenna	NI PXIe SDR platform	2.52 GHz	20 MHz	103 dB	122.6 Mbps 64-QAM	–	1.9
2016 [12]	Circulator-based single antenna	NI PXIe-5645R vector signal transceiver	2.46 GHz	80 MHz	Receiver noise floor	–	–	–
This work	Orthogonally-polarized slot antennas	ADI FMCOMMS1 FPGA real-time cancellation	3.5 GHz	184 MHz (SC) 123 MHz (SC) 81.4 MHz (OFDM)	70 dB 72.5 dB 76.4 dB	1474.56 Mbps 2 m 983.04 Mbps 3 m 884.74 Mbps 3 m	-25 dB -26.5 dB -23.2 dB	2

node and remote node at 300 cm distance. The achieved total throughput of 1474.56 Mbps is obtained when a 122.88 MBaud 64-QAM modulated signal is transmitted by both the local node and remote node at 200 cm distance. The corresponding low EVM values enable a throughput gain of 2 (in FD mode, the constellations of 64-QAM modulated signals are all detectable for different distances) or an average rate of 8 bits/s/Hz. As for OFDM signals, the achieved throughput is about 884.74 Mbps at 300 cm distance with -23.2 dB EVM. The achieved overall system performance in different environments and test conditions has already proven that, even though analog RF (baseband) cancellation is absent, the overall SI cancellation capability is sufficient to enable a high-throughput short-reach wireless full-duplex communication link in indoor environments.

C. Comparison to State-of-the-Art

Table I provides an overview of relevant publications on wireless full-duplex including measurement results. First of all, there are only a few publications demonstrating real-time self-interference cancellation. Besides, the other existing works target conventional wireless communications, where the signal of interest undergoes large path loss. In these publications, the maximal digital cancellation capability is achieved when the signal of interest is absent. In contrast, this work employs no training sequence for both the SI channel estimation and the detection of the signal of interest. In addition, there is no separate SI channel estimation period, meaning that the SI channel estimation and the desired signal detection are conducted simultaneously. This requires the communication systems to tolerate the degradation in self-interference digital cancellation due to the presence of the signal of interest. Another key challenge tackled by this work was achieving self-interference cancellation for a wideband frequency selective and time-variant channel. Meanwhile, the achieved total throughput exceeds that of other publications by taking advantages of a point-to-point short-reach communication link (where a LOS path is guaranteed). As discussed previously, the low transmit power mitigates the nonlinear distortions and hence simplifies the SI cancellation by reducing the necessity for analog cancellation, however, it also limits the coverage range of the FD communications for a given receiver noise floor and SNIR.

VI. CONCLUSION

This paper provides insight into a specific case of wireless full-duplex communications, being wideband short-reach full-duplex communication. The FPGA baseband design focuses on blind digital self-interference cancellation in the presence of a signal of interest on a frequency selective and time-varying channel. It is experimentally confirmed that the self-interference channel estimation can be performed with no knowledge of the signal of interest and the self-interference signal itself, and that the pre-estimation of the self-interference channel is not always necessary in such systems. This offers better bandwidth and time efficiency since neither the training data nor the separate calibration time is required to estimate the self-interference channel. The currently achieved performance demonstrates the practical feasibility of such communication systems using only a combination of antenna isolation and digital cancellation. This combined technique offers up to 72.5 dB cancellation for a wide signal bandwidth of 123 MHz when the signal of interest is absent. When both communication parties are transmitting, the achieved low EVM values can still support a high-data-rate communication link: up to 983.04 Mbps at 300 cm distance (at -26.5 dB EVM) or 1474.56 Mbps at 200 cm distance (at -25 dB EVM) for single-carrier signals, and up to 884.74 Mbps at 300 cm distance (at -23.3 dB EVM) for OFDM signals. These measurement results corroborate that, over short transmission distances, the impact of self-interference can be reduced to the level where the signal reception quality is not severely compromised.

REFERENCES

[1] S. Hong *et al.*, "Applications of self-interference cancellation in 5G and beyond," *IEEE Commun. Mag.*, vol. 52, no. 2, pp. 114–121, Feb. 2014.
[2] D. Kim, H. Lee, and D. Hong, "A survey of in-band full-duplex transmission: From the perspective of PHY and MAC layers," *IEEE Commun. Surveys Tuts.*, vol. 17, no. 4, pp. 2017–2046, 4th Quart., 2015.
[3] J. G. Andrews *et al.*, "What will 5G be?" *IEEE J. Sel. Areas Commun.*, vol. 32, no. 6, pp. 1065–1082, Jun. 2014.
[4] Q. Li, H. Li, P. Russell, Z. Chen, and C. Wang, "CA-P2P: Context-aware proximity-based peer-to-peer wireless communications," *IEEE Commun. Mag.*, vol. 52, no. 6, pp. 32–41, Jun. 2014.

[5] D. Burghal and A. F. Molisch, "Efficient channel state information acquisition for device-to-device networks," *IEEE Trans. Wireless Commun.*, vol. 15, no. 2, pp. 965–979, Feb. 2016.

[6] G. Torfs *et al.*, "ATTO: Wireless networking at fiber speed," *J. Lightw. Technol.*, vol. 36, no. 8, pp. 1468–1477, Apr. 15, 2018.

[7] *Wireless USB from the USB-IF*. Accessed: Oct. 19, 2017. [Online]. Available: http://www.usb.org/developers/wusb/

[8] A. Sabharwal, P. Schniter, D. Guo, D. W. Bliss, S. Rangarajan, and R. Wichman, "In-band full-duplex wireless: Challenges and opportunities," *IEEE J. Sel. Areas Commun.*, vol. 32, no. 9, pp. 1637–1652, Sep. 2014.

[9] Z. Zhang, K. Long, A. V. Vasilakos, and L. Hanzo, "Full-duplex wireless communications: Challenges, solutions, and future research directions," *Proc. IEEE*, vol. 104, no. 7, pp. 1369–1409, Jul. 2016.

[10] M. Chung, M. S. Sim, J. Kim, D. K. Kim, and C.-B. Chae, "Prototyping real-time full duplex radios," *IEEE Commun. Mag.*, vol. 53, no. 9, pp. 56–63, Sep. 2015.

[11] D. Korpi, M. Heino, C. Icheln, K. Haneda, and M. Valkama, "Compact inband full-duplex relays with beyond 100 dB self-interference suppression: Enabling techniques and field measurements," *IEEE Trans. Antennas Propag.*, vol. 65, no. 2, pp. 960–965, Feb. 2017.

[12] D. Korpi *et al.*, "Full-duplex mobile device: Pushing the limits," *IEEE Commun. Mag.*, vol. 54, no. 9, pp. 80–87, Sep. 2016.

[13] D. Bharadia, E. McMilin, and S. Katti, "Full duplex radios," *ACM SIGCOMM Comput. Commun. Rev.*, vol. 43, no. 4, pp. 375–386, Sep. 2013.

[14] Y.-S. Choi and H. Shirani-Mehr, "Simultaneous transmission and reception: Algorithm, design and system level performance," *IEEE Trans. Wireless Commun.*, vol. 12, no. 12, pp. 5992–6010, Dec. 2013.

[15] B. Debaillie *et al.*, "RF self-interference reduction techniques for compact full duplex radios," in *Proc. IEEE 81st Veh. Technol. Conf. (VTC Spring)*, May 2015, pp. 1–6.

[16] L. Laughlin, M. A. Beach, K. A. Morris, and J. L. Haine, "Electrical balance duplexing for small form factor realization of in-band full duplex," *IEEE Commun. Mag.*, vol. 53, no. 5, pp. 102–110, May 2015.

[17] E. Everett, A. Sahai, and A. Sabharwal, "Passive self-interference suppression for full-duplex infrastructure nodes," *IEEE Trans. Wireless Commun.*, vol. 13, no. 2, pp. 680–694, Jan. 2014.

[18] K. E. Kolodziej, B. T. Perry, and J. G. McMichael, "Multitap RF canceller for in-band full-duplex wireless communications," *IEEE Trans. Wireless Commun.*, vol. 15, no. 6, pp. 4321–4334, Jun. 2016.

[19] Y. Liu, X. Quan, W. Pan, and Y. Tang, "Digitally assisted analog interference cancellation for in-band full-duplex radios," *IEEE Commun. Lett.*, vol. 21, no. 5, pp. 1079–1082, May 2017.

[20] M. Duarte *et al.*, "Design and characterization of a full-duplex multiantenna system for WiFi networks," *IEEE Trans. Veh. Technol.*, vol. 63, no. 3, pp. 1160–1177, Mar. 2014.

[21] S. Li and R. D. Murch, "An investigation into baseband techniques for single-channel full-duplex wireless communication systems," *IEEE Trans. Wireless Commun.*, vol. 13, no. 9, pp. 4794–4806, Sep. 2014.

[22] M. S. Sim, M. Chung, D. Kim, J. Chung, D. K. Kim, and C.-B. Chae, "Nonlinear self-interference cancellation for full-duplex radios: From link-level and system-level performance perspectives," *IEEE Commun. Mag.*, vol. 55, no. 9, pp. 158–167, Jun. 2017.

[23] M. Duarte and A. Sabharwal, "Full-duplex wireless communications using off-the-shelf radios: Feasibility and first results," in *Proc. Conf. Rec. 40th Asilomar Conf. Signals Syst. Comput.*, Nov. 2010, pp. 1558–1562.

[24] A. Sahai, G. Patel, C. Dick, and A. Sabharwal, "On the impact of phase noise on active cancelation in wireless full-duplex," *IEEE Trans. Veh. Technol.*, vol. 62, no. 9, pp. 4494–4510, Nov. 2013.

[25] X. Quan, Y. Liu, S. Shao, C. Huang, and Y. Tang, "Impacts of phase noise on digital self-interference cancellation in full-duplex communications," *IEEE Trans. Signal Process.*, vol. 65, no. 7, pp. 1881–1893, Apr. 2017.

[26] V. Syrjala, M. Valkama, L. Anttila, T. Riihonen, and D. Korpi, "Analysis of oscillator phase-noise effects on self-interference cancellation in full-duplex OFDM radio transceivers," *IEEE Trans. Wireless Commun.*, vol. 13, no. 6, pp. 2977–2990, Jun. 2014.

[27] E. Ahmed and A. M. Eltawil, "On phase noise suppression in full-duplex systems," *IEEE Trans. Wireless Commun.*, vol. 14, no. 3, pp. 1237–1251, Mar. 2015.

[28] D. Korpi, T. Riihonen, V. Syrjälä, L. Anttila, M. Valkama, and R. Wichman, "Full-duplex transceiver system calculations: Analysis of ADC and linearity challenges," *IEEE Trans. Wireless Commun.*, vol. 13, no. 7, pp. 3821–3836, Jul. 2014.

[29] E. Ahmed, A. M. Ettawil, and A. Sabharwal, "Self-interference cancellation with nonlinear distortion suppression for full-duplex systems," in *Proc. 47th Asilomar Conf. Signals, Syst. Comput.*, Nov. 2013, pp. 1199–1203.

[30] S. K. Sharma, T. E. Bogale, L. B. Le, S. Chatzinotas, X. Wang, and B. Ottersten, "Dynamic spectrum sharing in 5G wireless networks with full-duplex technology: Recent advances and research challenges," *IEEE Commun. Surveys Tuts.*, vol. 20, no. 1, pp. 674–707, 1st Quart., 2018.

[31] S. Lemey *et al.*, "Threefold rotationally symmetric SIW antenna array for ultra-short-range MIMO communication," *IEEE Trans. Antennas Propag.*, vol. 64, no. 5, pp. 1689–1699, May 2016.

[32] R. A. Shafik, M. S. Rahman, and A. R. Islam, "On the extended relationships among EVM, BER and SNR as performance metrics," in *Proc. Int. Conf. Elect. Comput. Eng.*, Dec. 2006, pp. 408–411.

[33] D. Korpi, Y.-S. Choi, T. Huusari, L. Anttila, S. Talwar, and M. Valkama, "Adaptive nonlinear digital self-interference cancellation for mobile inband full-duplex radio: Algorithms and RF measurements," in *Proc. IEEE Global Commun. Conf. (GLOBECOM)*, Dec. 2015, pp. 1–7.

[34] D. Korpi, L. Anttila, and M. Valkama, "Impact of received signal on self-interference channel estimation and achievable rates in in-band full-duplex transceivers," in *Proc. 48th Asilomar Conf. Signals, Syst., Comput.*, Nov. 2014, pp. 975–982.

[35] D. Korpi, L. Anttila, and M. Valkama, "Reference receiver based digital self-interference cancellation in MIMO full-duplex transceivers," in *Proc. IEEE Global Commun. Conf. (GLOBECOM) Workshops*, Dec. 2014, pp. 1001–1007.

[36] J. G. Proakis and M. Salehi, *Digital Communications*, 5th ed. New York, NY, USA: McGraw-Hill, 2008.

[37] G. Q. Luo, Z. F. Hu, W. J. Li, X. H. Zhang, L. L. Sun, and J. F. Zheng, "Bandwidth-enhanced low-profile cavity-backed slot antenna by using hybrid SIW cavity modes," *IEEE Trans. Antennas Propag.*, vol. 60, no. 4, pp. 1698–1704, Apr. 2012.

[38] S. Lemey, O. Caytan, D. Vande Ginste, P. Demeester, H. Rogier, and M. Bozzi, "SIW cavity-backed slot (multi-)antenna systems for the next generation IoT applications," in *Proc. IEEE Topics Conf. Wireless Sensors Sensor Netw. (WiSNet)*, Jan. 2016, pp. 75–77.

[39] M. Duarte, C. Dick, and A. Sabharwal, "Experiment-driven characterization of full-duplex wireless systems," *IEEE Trans. Wireless Commun.*, vol. 11, no. 12, pp. 4296–4307, Dec. 2012.

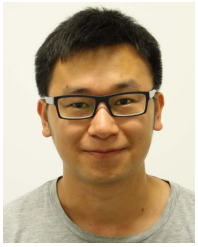

Haolin Li (S'15) received the M.S. degree in electronics engineering from Ghent University, Ghent, Belgium, in 2014. He is currently pursuing the Ph.D. degree in wireless communication and radio-over-fiber with the IDLab Research Group, Department of Information Technology (INTEC), Ghent University. His research interests include signal processing and digital circuit design for 5G and Internet of Things.

Joris Van Kerrebrouck (S'14) was born in Ghent, Belgium, in 1989. He received the M.S. degree in electronics engineering from Ghent University, Ghent, in 2014. He is currently pursuing the Ph.D. degree in high-speed electrical optical transceivers with the IDLab Design Group, Ghent University. His current research interests include radio over fiber, point-to-point optical links, and nonlinear electro-optical systems.

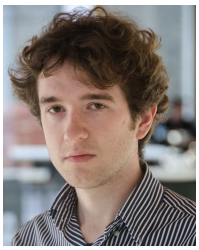

Olivier Caytan (S'17) received the M.S. degree in electrical engineering from Ghent University, Ghent, Belgium, in 2014, where he is currently pursuing the Ph.D. degree with the Electromagnetics Group, Department of Information Technology (INTEC). His research interests include the design of low-profile antennas for seamless integration in their surroundings and codesign of these antennas with active (opto)electronics.

Hendrik Rogier (SM'06) received the M.Sc. and Ph.D. degrees in electrical engineering from Ghent University, Ghent, Belgium, in 1994 and 1999, respectively. From 2003 to 2004, he was a Visiting Scientist with the Mobile Communications Group, Vienna University of Technology. He is currently a Full Professor with the Department of Information Technology, Ghent University, a Guest Professor at imec, Ghent, and a Visiting Professor with the University of Buckingham, Buckingham, U.K. He has authored and co-authored over 150 papers in international journals and over 170 contributions in conference proceedings. His current research interests include antenna systems, radiowave propagation, body-centric communication, numerical electromagnetics, electromagnetic compatibility, and power/signal integrity. Within the IEEE Microwave Theory and Techniques Society, he is a member of the Technical Committee 24 on RFID technology, and within the European Microwave Association, he is a member of the Governing Board of Topical Group MAGEO on Microwaves in Agriculture, Environment and Earth Observation. He was a recipient of the URSI Young Scientist Award twice at the 2001 URSI Symposium on Electromagnetic Theory and the 2002 URSI General Assembly. In addition, he was recipient of the 2014 Premium Award for Best Paper in *IET Electronics Letters*, the Best Paper Award's first place at the 2016 IEEE MTT-S Topical Conference on Wireless Sensors and Sensor Networks, the Best Poster Paper Award at the 2012 IEEE Electrical Design of Advanced Packaging and Systems Symposium, the Best Paper Award at the 2013 IEEE Workshop on Signal and Power Integrity, and the Joseph Morrissey Memorial Award for the First Best Scientific Paper at the 2013 Joint Meeting of the Bioelectromagnetics Society and the European BioElectromagnetics Association. He acts as the International Union of Radio Science (URSI) Commission B Representative for Belgium. He is an Associate Editor of *IET Electronics Letters*, *IET Microwaves, Antennas and Propagation*, and the IEEE TRANSACTIONS ON MICROWAVE THEORY AND TECHNIQUES.

Johan Bauwelinck (M'02–SM'18) was born in Sint-Niklaas, Belgium, in 1977. He received the Ph.D. degree in applied sciences and electronics from Ghent University, Ghent, Belgium, in 2005. Since 2009, he has been a Professor with the IDLab Research Group, Department of Information Technology (INTEC), Ghent University, where he has been leading the Design Lab since 2014. He became a Guest Professor at iMinds in 2014 and imec in 2016. He was/is active in the European-Union-funded projects GIANT, POWERNET, PIEMAN, EuroFOS, C3-PO, Mirage, Phoxtrot, Spirit, Flex5Gware, Teraboard, Streams, WIPE, and Optima, conducting research on advanced electronic integrated circuits for next-generation transport, metro, access, datacenter, and radio-over-fiber networks. He has promoted 18 Ph.D. students and co-authored over 200 publications. He holds 10 patents in high-speed electronics and fiber-optic communications. His research interests include high-speed high-frequency (opto-)electronic circuits and systems and their applications on chip and board level, including transmitter and receiver analog front-ends for wireless, wired and fiber-optic communication, or instrumentation systems. He is a member of the ECOC Technical Program Committee.

Piet Demeester (F'09) is currently a Professor with Ghent University–imec, Ghent, Belgium, where he is also the Department Director of the IDLab. He has co-authored over 1000 international publications. He holds an advanced ERC Grant. His research interests include distributed intelligence in the Internet of things, machine learning and data mining, semantic intelligence, cloud and big data infrastructures, fixed networking, wireless networking, electromagnetics, and high-frequency design.

Guy Torfs (M'13) received the Engineering degree in applied electronics and the Ph.D. degree in applied sciences and electronics from Ghent University, Ghent, Belgium, in 2007 and 2012 respectively. Since 2011, he has been with imec, associated with Ghent University, where he became an Assistant Professor in 2015. His research interests include high-speed mixed-signal designs for wireless baseband and fiber-optic and backplane communication systems, including digital signal processing and calibration, analog equalization circuits, and clock and data recovery systems. In 2014, as part of the Bi-PON and Cascaded Bi-PON team, he was a recipient of the Greentouch 1000x Award. He was a co-recipient of the 2015 DesignCon Best Paper Award in the High-Speed Signal Design Category. He serves as an Associate Editor for the IEEE TCAS-II and IEICE Elex.